materials

MDPI

Article

Design of SnO_2 Aggregate/Nanosheet Composite Structures Based on Function-Matching Strategy for Enhanced Dye-Sensitized Solar Cell Performance

Dongting Wang *, Shangheng Liu, Mingfa Shao, Jinghan Zhao, Yukun Gu, Qiuyi Li, Xianxi Zhang, Jinsheng Zhao and Yuzhen Fang

Shandong Provincial Key Laboratory of Chemical Energy Storage and Novel Cell Technology, School of Chemistry and Chemical Engineering, Liaocheng University, Liaocheng 252059, China; liush@lcu.edu.cn (S.L.); shaomf@lcu.edu.cn (M.S.); zhaojh@lcu.edu.cn (J.Z.); guyk@lcu.edu.cn (Y.G.); liqy@lcu.edu.cn (Q.L.); zhangxianxi@lcu.edu.cn (X.Z.); zhaojinsheng@lcu.edu.cn (J.Z.); fangyuzhen@lcu.edu.cn (Y.F.)

* Correspondence: wangdongting@lcu.edu.cn or wdtcell@126.com; Tel.: +86-635-823-0680

Received: 12 August 2018; Accepted: 11 September 2018; Published: 19 September 2018

Abstract: Hierarchical SnO_2 nanocrystallites aggregates (NAs) were prepared with a simple room temperature–based aqueous solution method followed by simple freeze-drying treatment. The as-prepared SnO_2 NAs were subsequently combined with SnO_2 nanosheet–based structures from the viewpoint of a function-matching strategy, and under an optimized condition, a power conversion efficiency (PCE) of 5.59% was obtained for the resultant hybrid photoanode, a remarkable 60% enhancement compared to that of dye-sensitized solar cells (DSCs) fabricated with bare SnO_2 NAs architecture. The significantly enhanced efficiency can be attributed to the combination of the desirable electron transport property obtained by the intentionally introduced SnO_2 nanosheets (NSs) and the effectively retained inherent characteristics of SnO_2 NAs, i.e., large surface area and strong light-scattering effect. This work provides a promising approach for the rapid development of highly efficient SnO_2 photoanode film-based DSCs with the properties of simplicity of operation and control over the photoanode composition.

Keywords: hierarchical SnO_2 aggregates; room temperature method; SnO_2 aggregate/nanosheet composite; photoanode; dye-sensitized solar cells

1. Introduction

Since the breakthrough work in mesoscopic dye-sensitized solar cells (DSCs) by O'Regan and Grätzel, a great deal of effort has been made on this unique device because of its advantages of being highly efficient and environmentally friendly, with low cost and ease of fabrication [1–3]. Apart from the most commonly studied photoanode material, TiO_2, alternative metal oxides such as SnO_2 have been widely investigated in the past decade. In contrast to TiO_2, SnO_2 has two outstanding advantages, a larger band gap (Eg = 3.6 eV) and faster mobility of charge carriers (~100–200 $cm^2V^{-1}s^{-1}$) within individual structures [4–6], which results in the long-term stability of DSCs and reduced charge recombination probability within the photoanode film. For SnO_2-based cells, the conventional photoanode film is generally composed of mesoporous nanoparticles, hence it provides a large surface area for sufficient dye loading. However, a major drawback to be overcome for such SnO_2-based DSCs is the severe charge carrier recombination losses in the electron transfer process as a result of various interfaces and grain boundaries [7–9]. In addition, the weak visible light-scattering capability of such porous photoanode has been proven to be another disadvantage, since a large portion of the incident light will directly pass through the small nanoparticle-based film without effective harvesting

and utilization [10,11]. As such, although SnO_2 nanoparticle-based DSCs have been extensively investigated, the conversion efficiencies are still much lower than those of TiO_2, making them less competitive. Therefore, how to effectively accelerate the electron transfer and enhance the visible light-scattering ability of SnO_2 photoanode film with retention of relatively high surface area is regarded as the key approach to attain DSCs with high conversion efficiency.

Integrating the small-sized nanoparticles into three-dimensional (3D) microstructures such as aggregates and hollow spheres has proven to be a promising strategy for efficiency enhancement, since the 3D structures not only offer large surface areas for sufficient dye molecule loading favored by the small size of the constructed building blocks, but also improve the light-scattering capability provided by these architectures, with tunable size ranging from hundreds of nanometers to micrometers [12–14]. To date, the DSCs assembled with specific 3D-nanostructure photoanode film has achieved the highest conversion efficiency of 8.21% after $TiCl_4$ treatment [15]. Nevertheless, small inner grains in the 3D structures and poor interconnectivity between these microarchitectures hinders electron transport within the photoanode film and thus inflicts charge recombination to some extent [16,17]. Compared with the 3D architectures, two-dimensional (2D) nanosheets (NSs) could provide straight electric pathways for faster charge transport due to their excellent electrical conductivity and increased electron diffusion length, thus preventing the recombination losses originating from the reaction between oxidizing dyes and photogenerated electrons [18,19]. However, the weak light-harvesting efficiency of these films, ascribed to the small specific surface area and moderate light-scattering capability, constrains their power conversion efficiency to relatively low levels [20,21]. Moreover, the 2D nanostructures can significantly agglomerate or be overlaid during the film preparation process, leading to reduced surface area and/or light-scattering capability. Actually, it has been established that the application of single component or morphology for photoanode film makes it hard to simultaneously satisfy the required properties—high specific surface area, outstanding light scattering, and fast electron transport—for efficient DSCs due to the intrinsic drawbacks of each element. With regard to these issues, substantial efforts have been focused on fabricating multidimensional hybrid photoanode nanomaterials, aiming to combine the desirable characteristics of each nanostructure. As an example, Yang et al. successfully formed SnO_2/TiO_2 heterostructure by incorporating 2D SnO_2 nanosheets into TiO_2 nanoparticle-based photoanodes and found that in this system, rapid electron transport pathways and improved light scattering were obtained from 2D SnO_2 nanosheets with the retention of sufficient dye-loading ability [22]. Moreover, Tao et al. reported a novel ZnO composite photoanode composed of 3D ZnO aggregates (NAs) and bridging 2D ZnO nanosheets (NSs) that yielded a near-record power conversion efficiency (PCE) of 7.35% because of the effective combination of the relatively strong light-scattering property of ZnO NAs with the increased surface area and favorable electron transport of ZnO NSs [23]. In line with these noteworthy features of the composite photoanode, SnO_2 hybrid photoanode consisting of function-matching structures shows great promise in dramatically enhancing DSC efficiency. However, to date, the design and investigation of SnO_2 hybrid photoanode has yet to be reported.

Herein, for the first time, SnO_2 NS–based 3D and 2D sheet composite architectures are intentionally introduced in 3D SnO_2 NAs film to construct hybrid SnO_2 architecture, within which 3D SnO_2 NAs act as building blocks to augment the accessible surface area for sufficient dye uptake and enhance light scattering for effective light utilization, while SnO_2 NSs mainly play the vital role of facilitating electron transport within the film. To coordinate the specific features of each component, the ratio of NAs to NSs is rationally tuned, and under optimum conditions, an enhanced photovoltaic conversion efficiency of 5.59% was obtained for the composite photoanode, showing a remarkable 60% increment in comparison with the DSC fabricated with bare SnO_2 NAs under the same conditions. Various measurements revealed that such outstanding performance of the resultant photoanode was ascribed to a reasonable combination of the excellent charge transport and strong light-harvesting capabilities resulting from the synergy of SnO_2 NAs architecture and SnO_2 nanosheet-based structures.

2. Experimental Section

2.1. Materials

Tert-butylpyridine (t-BPy), 3-methoxypropionitrile, iodide (I_2), anhydrous lithium iodide (LiI), and 2,3-dimethyl-1-propyl imidazolium iodide (DMPII) were purchased from (Sigma, St. Louis, MO, USA). Na_2CO_3, SnF_2, $SnCl_2{\cdot}2H_2O$, $C_6H_{12}N_4$ (methenamine), $TiCl_4$, and $H_2PtCl_6{\cdot}6H_2O$ were all obtained from commercial sources and used without further treatment. The popular dye sensitizer [cis-bis(isothiocyanato)bis-(2,2-bipyridyl-4,4-dicarboxylato) ruthenium (II) bis(tetrabutyl-ammonium)] was purchased from (Dyesol, New South Wales, Australia).

2.2. Preparation of SnO_2 Aggregates

SnO_2 aggregates were prepared by hydrolyzing $SnCl_2$ at room temperature, followed by freeze-drying. In a typical synthesis, 1.128 g $SnCl_2{\cdot}2H_2O$ was first dissolved in deionized water (40 mL) under magnetic stirring, followed by the slow addition of 1.25 mM Na_2CO_3. Still at room temperature, the resultant white suspension was continuously stirred for 7 days, leading to the formation of homogeneous SnO_2 solution. Afterwards, the resulting solution was subjected to freeze-drying for 24 h, followed by repeated centrifugation/sonication/dispersion in water 5 times. After drying at 80 °C for 4 h in air, SnO_2 aggregates were finally obtained.

2.3. Preparation of SnO_2 Nanosheets

SnO_2 NSs were prepared with a hydrothermal method similar to the literature reported by other groups [19]. Typically, 0.047 g SnF_2 was first dissolved in deionized water (30 mL), followed by the addition of 0.035 g methenamine under magnetic stirring. After stirring for 30 min, the obtained white turbid suspension was transferred into a Teflon-lined stainless steel autoclave (60 mL) and heated at 180 °C for 12 h in an electric oven. After being cooled to room temperature, the obtained brown suspension was repeatedly washed with deionized water and ethanol by centrifugation at a rate of 9000 rpm for 10 min. Finally, the product was harvested and dried at 60 °C overnight under ambient conditions.

2.4. Preparation of SnO_2 Hybrid Photoanode and Cell Assembly

The SnO_2 hybrid electrode was formed by coating SnO_2 composite on precleaned fluorine-doped tin oxide (FTO)-coated glass plates (Nippon, Tokyo, Japan, 7 Ω/sq) in conjunction with a programmed annealing procedure [24]. As an example, 50 wt% (the content of NS in the mixture) SnO_2 hybrid photoanode film was obtained as follows: NAs and NSs with a total weight of 0.2 g were dispersed into a mixture of ethyl cellulose (0.1 g), terpineol (0.6 g), ethanol (2 mL), and acetic acid (0.04 mL), followed by grounding for approximately 60 min. The obtained viscous paste was spread uniformly on FTO substrate with the typical doctor-blading technique. The thickness of the films was controlled by the layers of tape adhered on the FTO substrate. For all samples, the same number of layers of adhesive tape was applied to ensure identical thickness of working electrodes. After being dried, the photoanode films were formed by gradually annealing in a programmed procedure, first at 325 °C for 5 min, then at 375 °C for 5 min, then at 450 °C for 15 min, and finally at 500 °C for 15 min. After that, the synthesized SnO_2 film was treated with 0.4 M $TiCl_4$ aqueous solution at 77 °C for 50 min, washed with water and ethanol to remove unanchored Ti source, and finally sintered at 450 °C for 2 h. In parallel, another 4 samples with different NS contents (0 wt%, 33 wt%, 67 wt%, and 100 wt%) were prepared under the identical synthesis procedures as described above. For simplicity, the above 5 as-prepared samples are denoted as TP, TPS1, TPS2, TPS3, and TPS4, respectively.

Dye sensitization was performed by soaking the resultant SnO_2 hybrid electrodes in 5.0×10^{-4} M N719 dye ethanolic solution for 24 h in the dark at room temperature. The Pt counter electrode was obtained by dropping 0.35 mM H_2PtCl_6/isopropanol solution on the FTO conductive substrate and subsequently annealing in a muffle furnace at 400 °C for 30 min under air flow conditions. The DSCs

were then assembled by bonding the sensitized photoanode (0.16 cm^2) and prepared Pt-coated counter electrode together with a hot-melt Surlyn film (25 μm thick; DuPont, Wilmington, DE, USA). The liquid electrolyte, consisting of 0.1 M LiI, 1.0 M DMPII, 0.12 M I_2, and 0.5 M t-BPy in 3-methoxypropionitrile, was filled into the whole internal space of the fabricated cells by vacuum backfilling.

2.5. Characterizations

XRD patterns were recorded from a D/MAX-rA diffractmeter (Rigaku, Tokyo, Japan) with a Cu Kα radiation source (λ = 0.15406 nm). The morphologies of the as-prepared SnO_2 NAs and NSs and the resultant hybrid films were examined with transmission electron microscopy (TEM, JEOL-2010, Hitachi, Tokyo, Japan) and field-emission scanning electron microscope (FESEM, JEOL-6701F, Akishima, Japan), respectively. The specific surface areas (S_{BET}) were analyzed based on nitrogen adsorption–desorption isotherms recorded with an Autosorb iQ-XR Analyzer (Quantachrome Instruments, Boynton Beach, FL, USA). Dye desorption experiments were conducted by immersing the photoanode films in 1.0 M NaOH in water/ethanol (50:50, *V*/*V*) solution, and the concentration of desorbed dye was quantitatively analyzed using an ultraviolet-visible (UV–vis) spectrophotometer (Cary 500, Varian, Palo Alto, CA, USA). The diffuse reflectance spectra of the films with various NS content were investigated with a QEX10 spectral response system from PV Measurements, Inc. The photoelectrochemical characterizations were performed by a Keithley Model 2400 source meter under simulated AM 1.5 G one-sun illumination (100 $mW \cdot cm^{-2}$, Newport Corporation, Los Angeles, CA, USA) with the sweep direction from forward to reverse. Before each test, the light intensity was first calibrated by a National Renewable Energy Laboratory (NREL) calibrated Si solar cell (PV Measurements, Inc., Boulder, CO, USA). Electrochemical impedance spectroscopy (EIS) experiments were performed under one-sun illumination using an electrochemical workstation (CHI760, CH Instruments, Shanghai, China) at V_{OC} with an AC modulation signal of 10 mV within a frequency range of 0.1–10^5 Hz.

3. Results and Discussion

3.1. XRD Patterns and BET Surface Area Analysis

The crystalline phases of both SnO_2 NAs and NSs were analyzed with X-ray diffraction (XRD) spectra. As shown in Figure 1a, it can clearly be seen that all the diffraction peaks of the products are well assigned to the tetragonal rutile structure of SnO_2 (JCPDS. 41–1445), and no other impurity is detected, suggesting the successful transformation from Sn^{2+} to SnO_2 during the room temperature stirring process. As reported by Xie et al., Sn^{2+} can be oxidized to Sn^{4+} in aqueous solution in the presence of oxygen, and the first formed amorphous phase can crystallize further at room temperature due to its inherently strong tendency to transform to crystalline structure [25,26]. Moreover, compared with the common SnO_2 samples suffering from high-temperature calcination, the synthesized product shows much broader diffraction peaks, indicating the small size of primary nanoparticles or building blocks in the as-prepared SnO_2 NA product. As calculated on the basis of Scherer's formula, the average crystallite size of the primary nanoparticles determined by the full width at half-maximum (FWHM) of the (110) peak is about 5 nm. The above morphological feature of SnO_2 NA finally enables the desired specific surface area. As shown in Figure 1b, N_2 adsorption and desorption isotherms evidence that SnO_2 NAs present an impressively high specific surface area of approximately 166.7 m^2/g, which is twice that of SnO_2 NSs (62.6 m^2/g), suggesting the potentially sufficient dye-anchoring ability of the resultant photoanodes.

3.2. Morphological and Composition Characterization

As can be seen from Supplementary Figure S1, the as-synthesized SnO_2 NAs show irregularly aggregated character with size ranging from about 100 nm to 5 μm. The amplified TEM image (see Figure 2a) distinctly evidences that the SnO_2 NAs are hierarchically composed of numerous tiny nanoparticles. The formation of specific features could result from the given ratio of $SnCl_2$ and Na_2CO_3

as suggested in our previous work [23]. Further HRTEM characterization, shown in Figure 2b, reveals clear lattice fringes of d = 0.26 and 0.34 nm, respectively, corresponding well to the lattice spacing of (101) and (110) planes of rutile SnO_2 lattice. Moreover, the crystal size demonstrated in the HRTEM image exhibits good consistency with the calculated data from the XRD characterization.

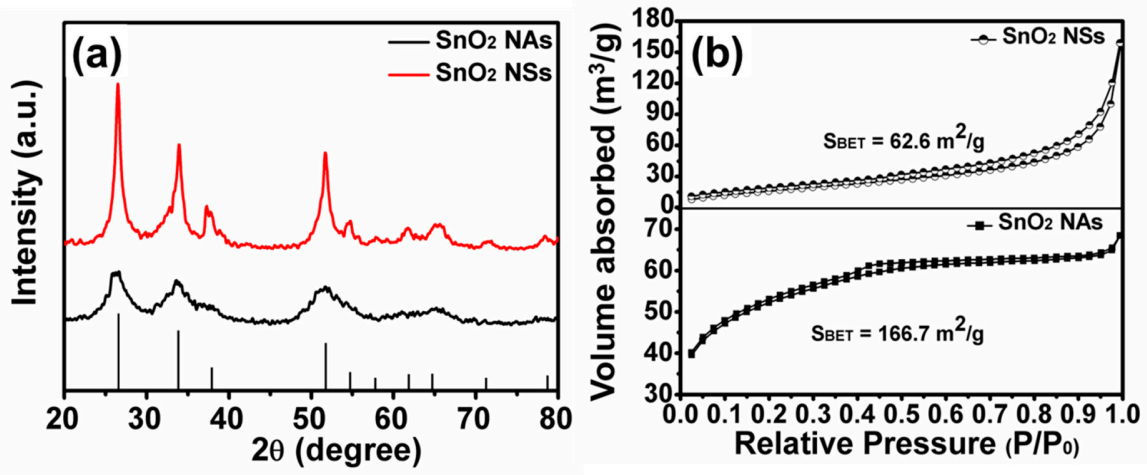

Figure 1. (**a**) XRD patterns of the as-prepared SnO_2 NAs and SnO_2 NSs. (**b**) Nitrogen adsorption and desorption isotherms of SnO_2 NAs and SnO_2 NSs. Vertical bars below represent the standard XRD pattern of SnO_2.

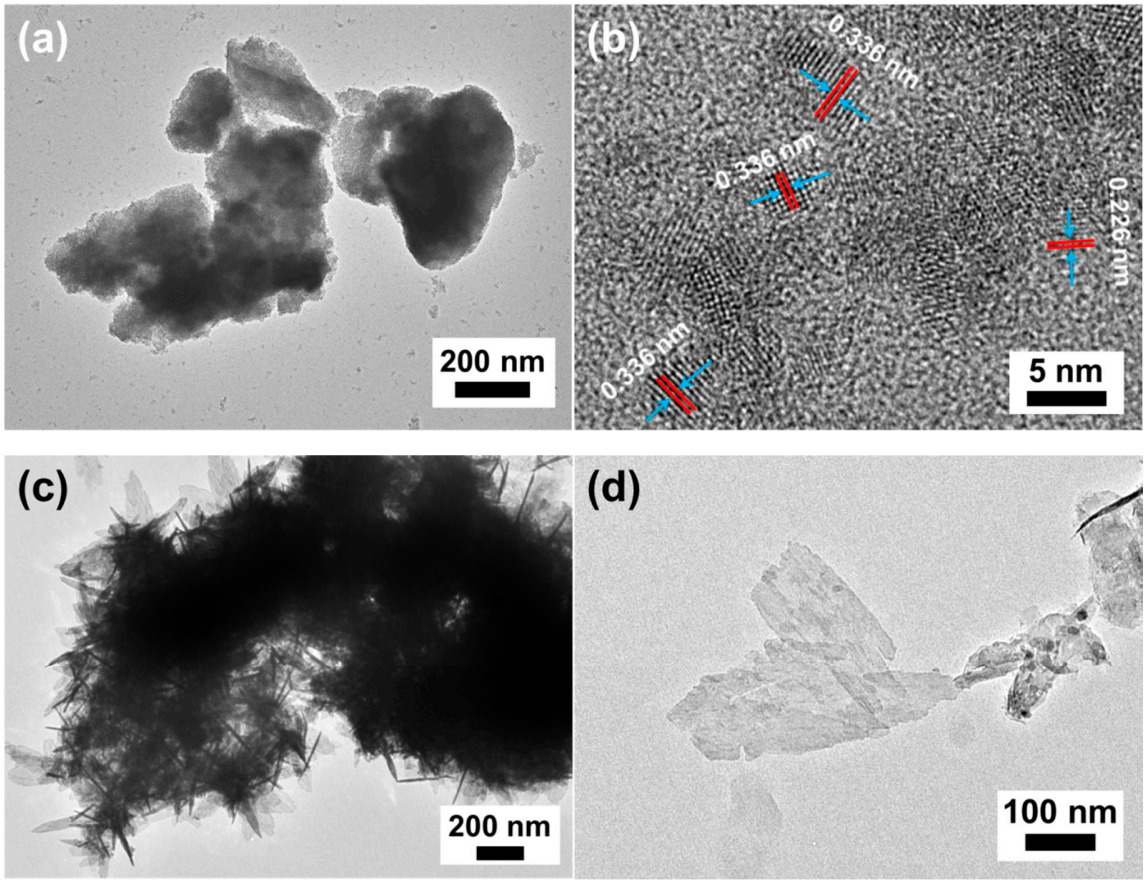

Figure 2. (**a**) TEM and (**b**) HRTEM images of synthesized SnO_2 NAs, and (**c**,**d**) TEM images of 3D structured SnO_2 NSs and random SnO_2 NSs.

Apart from SnO_2 NAs, another typical nanostructure, SnO_2 NSs, was also synthesized and the morphology of the product was characterized. As demonstrated in Figure 2c, the typical TEM image proves the successful formation of tightly interconnected nanosheets based on a flower-like 3D hierarchical structure. These outstanding features should be not only favorable for the penetration of liquid electrolyte due to the formation of a highly open and porous structure, but also advantageous for light scattering due to the comparable size of SnO_2 NSs with the wavelength of the incident light [27]. More interestingly, random 2D SnO_2 nanosheets with high transparency are also obtained (see Figure 2d). Such morphological characteristics indicate that the formed nanosheets could effectively connect the SnO_2 NAs framework and serve as an electron transport highway, thus shortening the diffusion pathways and lengthening the diffusion distance [22,28].

After mixing the synthesized SnO_2 NAs together with the SnO_2 NSs, hybridized films with and without $TiCl_4$ treatment were fabricated, and the corresponding SEM images are displayed in Figure 3. It can be seen from Figure 3a that both hierarchical SnO_2 NSs and SnO_2 NAs can be easily visualized before $TiCl_4$ treatment, implying the well-preserved inherent characteristics of each composition. Further observation reveals that not only hierarchical SnO_2 NSs but also 2D SnO_2 NSs can be clearly seen inside the SnO_2 hybridized film (see Figure 3c), which is consistent with the above TEM characterization. As can be seen in Figure 3b,d, after $TiCl_4$ treatment, the surface of the TPS2 becomes obviously rougher and the size seems much larger in comparison with untreated film, indicating the significant influence of $TiCl_4$ post treatment on the SnO_2 film structure. However, it is worth noting that even after being subjected to $TiCl_4$ treatment, the hierarchical architecture is maintained. Additionally, a discernible detached sheet without complete coverage after $TiCl_4$ treatment can be clearly observed, further confirming the presence of SnO_2 NSs in the TiO_2-coated SnO_2 hybrid film.

To probe the composition of the TSP2 film, the typical XPS survey spectrum was collected. As shown in Figure 3c, the appearance of peaks corresponding to Ti, O, and Sn demonstrates the successful coating of TiO_2 on the SnO_2 surface. In addition, the high-resolution XPS spectrum with scanning over the above Ti element was conducted and the result is depicted in Figure 3d. Notably, the Ti 2p XPS spectrum shows two typical peaks at 458.4 eV and 464.2 eV, corresponding to the binding energies of different Ti^{4+} states, i.e., Ti 2p 3/2 and Ti 2p 1/2, respectively [29,30].

3.3. Photocurrent Density—Voltage Characteristics

The photovoltaic performance of DSCs with different NS content was measured under AM 1.5 sunlight illumination (100 mW cm^{-2}). The results are given in Figure 4 in the form of representative J–V curves, and detailed photovoltaic parameters (J_{SC}, V_{OC}, PCE, and fill factor (FF)) are shown in Table 1. As can be seen from Figure 4, the sample without NS (sample TP) exhibits a relatively high J_{SC} of 15.12 mA cm^{-2} but a low V_{OC} of 0.537 V and a FFof 0.43. This observation can be associated with the component of the working electrode. As revealed in Figure 2a, the as-prepared hierarchically structured SnO_2 NAs most likely possess strong light-scattering effect and sufficient dye-loading capability, thus promoting photon absorption to enhance the J_{SC} value. However, the low V_{OC} and FF in turn illustrate the intrinsic disadvantage of the as-prepared SnO_2 NAs. In contrast, the pure SnO_2 NS–based DSC (TPS4) prepared under identical conditions shows adverse characteristics, with a high V_{OC} of 0.693 V and an impressive FF of 0.68, but a small J_{SC} of 6.59 mA cm^{-2}. As reported previously, the V_{OC} could probably change with altered morphologic and/or crystallographic orientation due to the shift of the Fermi level [31–33]. As a typical low-index crystal facet with fewer crystal edges and defects, nanosheets could bring about increased electron density in the conduction band because of the decreased electron−hole recombination arising from the excellent electron transport property of the specific structure, thus making the negative shift of the Fermi level position. In view of the prominent advantage of nanosheets, the great improvement in photovoltaic performance is worth looking at for NSs containing hybrid structure. As expected, with the increase of NS content from 0% to 50%, the key parameters of the cells, namely TPS1 and TPS2, improve gradually, leading to a continuous increment of PCE from 3.50% to 5.59%. However, when the NS content is further increased,

sample TPS3 shows drastically decreased J_{SC} and PCE (J_{SC}: 11.46 mA cm^{-2}; PCE: 4.48%). The above observation can be explained as follows: though the NS-based structures in the photoanode film can act as bridges to connect the interparticles, the increased NS in the hybrid film could also result in a gradual decrease of the dye-loading amount owing to their lower specific surface area as compared to SnO_2 NAs, leading to a gradual reduction of light-harvesting capability. Consequently, when the improved electron transfer property cannot compensate the loss of surface area, low J_{SC} and PCE are expected. Therefore, it can be deduced that controlling the content of NS in the composite film is important for reasonable coordination of electron transport and light harvesting.

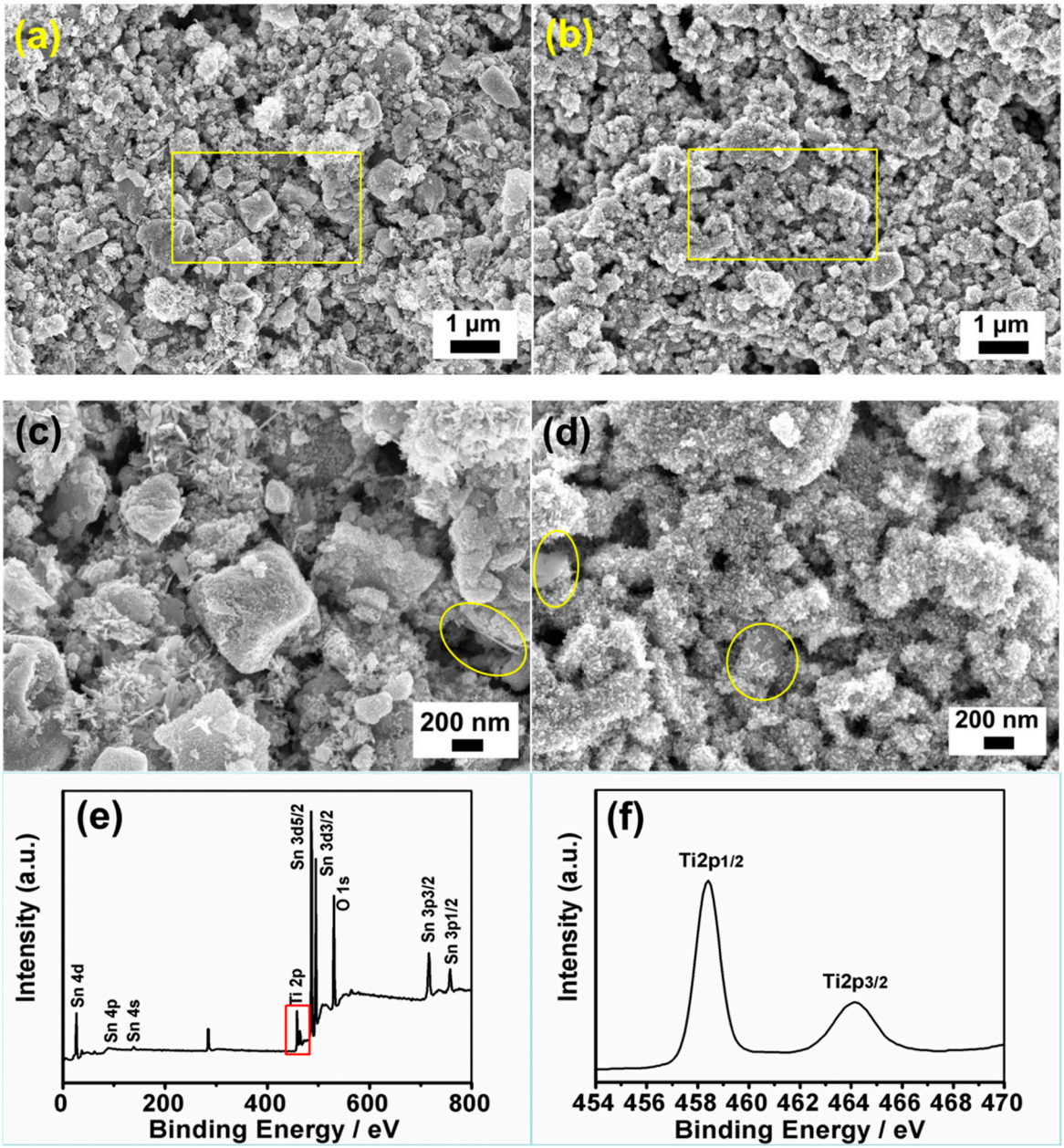

Figure 3. SEM images of SnO_2 NA/NS hybrid films (**a**,**c**) before and (**b**,**d**) after $TiCl_4$ treatment with different modifications; XPS spectra of (**e**) survey and (**f**) Ti 2p peaks.

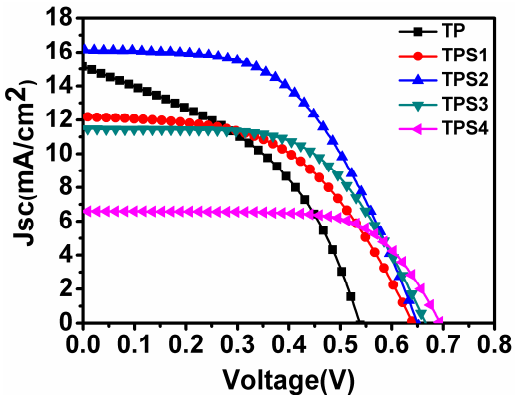

Figure 4. J–V characteristic curves of various DSCs based on TP, TPS1, TPS2, TPS3, and TPS4.

Table 1. Characteristics of the SnO_2 photoanodes together with the corresponding photovoltaic parameters. FF, PCE, power conversion efficiency.

Sample	J_{SC} (mA/cm^2)	V_{OC} (V)	FF	PCE	Adsorbed Dye ($\times 10^{-7}$ mol·cm^{-2})	R_{ct}
TP	15.12	0.537	43.1	3.50	1.94	38.9
TPS1	14.61	0.640	51.6	4.85	2.23	27.8
TPS2	16.14	0.650	53.3	5.59	2.07	18.5
TPS3	11.46	0.665	58.8	4.48	1.76	11.6
TPS4	6.59	0.693	68.1	3.11	1.15	9.8

3.4. Dye Absorption and Diffuse Reflectivity

To reveal the mechanism behind the improved photovoltaic performance of the hybrid structure DSCs, the dye uptake in all photoanodes was studied. As shown in Table 1, the dye adsorption ability of the resultant SnO_2 films is largely dependent on the NS content. Specifically, the dye-loading amount first increases from 1.94×10^{-7} mol cm^{-2} to 2.23×10^{-7} mol cm^{-2} by increasing the NS content from 0% to 33%, and then decreases from 2.07×10^{-7} mol cm^{-2} to 1.76×10^{-7} mol cm^{-2} when the NS content is increased from 50% to 67%. Another reference photoanode film, TPS4, displayed the lowest dye-loading amount, 1.15×10^{-7} mol cm^{-2}. This significant variation in dye absorption could be explained as follows: on the one hand, the introduced SnO_2 NSs likely disperse between SnO_2 NAs (see Figure 3c) and inhibit their aggregation; on the other hand, the presence of SnO_2 NAs could also retard the undesired overlap of the SnO_2 NSs. Therefore, the hybrid structure with proper SnO_2 NSs could offer sufficient contact area for TiO_2 deposition or coating, which would lead to a large amount of dye absorption. However, further augmenting the content could result in severe stacking of SnO_2 NSs, leading to reduced surface area.

To investigate the influence of SnO_2 NSs on the scattering effect of the hybrid structures, the reflectivity of each photoanode film was studied, shown in Figure 5. Apparently, TP has the highest diffuse reflection, in the range of 400 nm to 800 nm, while TS shows the lowest reflectance in the same region, which actually is consistent with our hypothesis on the more effective incident light-scattering ability of SnO_2 NAs. As for the hybrid film, increasing the amount of SnO_2 NSs from TPS1 to TPS3 generated gradually weakened light-scattering capabilities in the entire visible light region. The obvious light reflectance intensity distinction must be ascribed to the inferior incident light-scattering capability of bare SnO_2 NSs compared to bare SnO_2 NAs. The above observation along with the dye desorption test confirm the outstanding features of SnO_2 NAs for sufficient dye absorption and excellent light scattering. However, as revealed in the photovoltaic test section, sample TPS2 rather than TP achieved the highest efficiency. Therefore, considering the mismatch between the moderate light-harvesting capability and the optimum photovoltaic performance, the significant increase in PCE of the TPS2 cell must stem from the favorable electron transport and effectively suppressed electron recombination within the film.

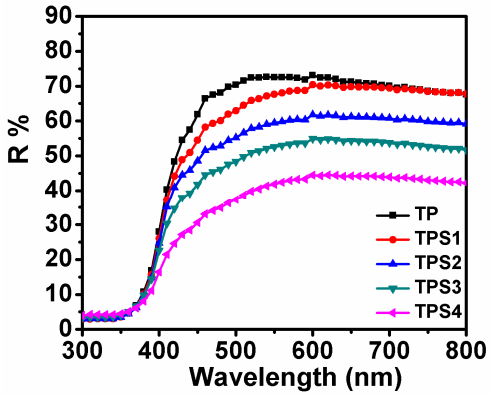

Figure 5. Diffuse reflectance spectra of the TP, TPS1, TPS2, TPS3, and TPS4 films.

3.5. EIS Analysis

Electrochemical impedance spectroscopy (EIS) analysis was employed to gain insight into the electrical behavior of DSCs based on SnO_2 NAs with and without NSs, with the aim of revealing the mechanism behind the differences in photovoltaic performance among all samples. Figure 6 shows the typical EIS Nyquist plots of all DSCs obtained under a simulated solar light of 100 mW cm^{-2} at a bias potential of V_{OC}. It can be seen that the EIS Nyquist plots have three well-defined semicircles in the corresponding regions, i.e., high frequency (>10^3 Hz), medium frequency (10^0-10^3 Hz), and low frequency (<10^0 Hz), which denote charge transfer resistance at the Pt counter electrode/electrolyte interface, recombination resistance at the SnO_2/dye/electrolyte interface, and the Warburg diffusion process of I^-/I_3^- in the electrolyte, respectively [1,34]. According to the approach of Adachi et al., the charge transfer recombination impedance (R_{ct}) in the photoanode can be deduced from the central semicircle of the Nyquist plot, and the corresponding resistance values can be determined by Zview software fitting [35]. As displayed in Table 1, it can be obviously seen that the charge transfer resistance of the resultant photoanodes decreases successively from 39.4 ohm for the TP to 10.2 ohm for the TPS4 cell with the increment of SnO_2 NS amount, implying slower electron recombination for the samples with higher SnO_2 NS content. This phenomenon is explainable, since the injected electrons could probably recombine with I_3^- in the electrolyte in the SnO_2 NA photoanode film before reaching the collector electrode (e.g., FTO substrate) due to the partial zigzag pathway for electron transfer. However, after the incorporation of SnO_2 NS nanostructures, the produced electron could pass through the photoanode film more easily due to the effective interconnectivity between the neighboring SnO_2 NAs and favorable electron transport route arising from SnO_2 NSs, thus promoting electron diffusion and collection efficiency.

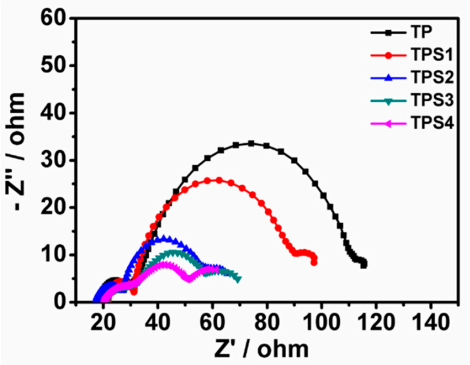

Figure 6. Nyquist plots of various SnO_2 photoanode films–based DSCs.

3.6. IPCE Spectra

Figure 7 shows the typical incident photon conversion efficiency (IPCE) spectra of various DSCs fabricated with bare SnO_2 NAs, SnO_2 NSs, and SnO_2 NAs/NSs hybrid photoelectrodes as a function of the illumination wavelength ranging from 400 nm to 800 nm, in which maximum intensities for all DSCs are observed at the wavelength of 530 nm, which is consistent with the absorption characteristic of the N719 molecule. For the hybrid structures, it can be seen that the IPCE value first increases and then decreases with the increment of NS; that is, the IPCE of TPS1 and TPS2 hybrid films is much higher than that of TP-based film in the whole visible wavelength range, while the IPCE of the TPS3 film is much lower, which coincides with the observed variation trend of J_{SC} as shown in Figure 4. Moreover, the highest IPCE value for TPS2 hybrid photoanode confirms the need to control the amount of NSs in the resultant film for marked improvement in the photovoltaic performance of DSCs. Generally, IPCE is regarded as a comprehensive result related to light-harvesting efficiency, electron-injection efficiency, and charge-collection efficiency [11,36,37]. However, in view of the same charge-injection efficiency for the studied SnO_2/dye system, it is reasonable to presume in this work that the IPCE improvement is closely related to light-harvesting and charge-collection efficiency of the photoanode film, the former of which is proportional to the dye-loading amount and light-scattering capability, while the latter is determined by the electron-transport property [38,39]. As for TPS1 and TPS2, considering their lower light-scattering capability compared with bare SnO_2 NA (sample TP), we believe that the higher IPCE is attributed to the significantly enhanced electron-collection efficiency and increased dye-loading amount. Regarding TPS3 and TPS4, the significantly decreased IPCE could be ascribed to the more remarkable reduction of dye loading and light scattering than the increase of electron-collection efficiency, as discussed above.

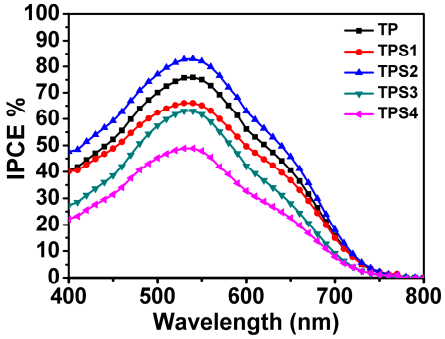

Figure 7. IPCE spectra of DSCs based on TP, TPS1, TPS2, TPS3, and TPS4.

3.7. Schematic Views of Electron Transfer and Recombination

When traveling across the SnO_2 photoanode, the incident light either transmits the film or is scattered by the semiconductor oxide film in addition to the part harvested by the sensitizer. As for the typical photoanode fabricated with SnO_2 NAs, the aggregates within the resultant film are generally submicrometer-sized and therefore are particularly effective scattering centers for visible light, giving rise to a striking increase in the light-harvesting property of the photoelectrode film. Meanwhile, since the aggregates are composed of closely packed primary nanocrystallites, the internal surface area is always reserved with the achievement of strong light-scattering capability. However, the electron transport along the 3D NAs is often retarded due to the poor interconnectivity between these microarchitectures, hence the transfer of photogenerated electrons to the conductive substrate for photocurrent extraction is not efficient (see Scheme 1a). As shown in Scheme 1b, the incorporation of NS-based architectures in the 3D NA film can not only effectively improve the interconnectivity between the aggregates but also provide additional high pathways, leading to a more favorable electron transport route and much longer diffusion length [40,41]. Therefore, the outstanding photovoltaic performance of the hybrid-based DSCs

could be attributed to synergy of the received fast electron transport property from SnO_2 NSs and the retained strong light harvesting and large surface area of SnO_2 NAs.

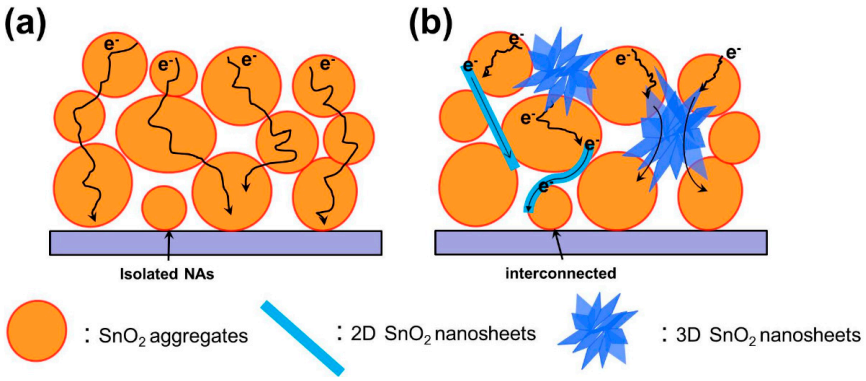

Scheme 1. Schematic illustration of electron (e^-) diffuse transport in (**a**) bare SnO_2 NAs photoanode film with irregular morphology and (**b**) SnO_2 NAs/NSs hybrid photoanode film.

4. Conclusions

In conclusion, a new type of SnO_2 hybrid structure, consisting of irregular 3D SnO_2 NAs and SnO_2 NSs based 3D and 2D architectures, was successfully fabricated based on a function-matching strategy and subsequently applied as a multifunctional photoanode for high-efficiency DSCs. Various materials and device characterizations, including reflectance spectra, dye-absorption ability, and EIS analysis, demonstrated that the SnO_2 hybrid films could synchronously possess the desirable features of each composition, i.e., the large dye-absorption amount and strong light-scattering property of 3D SnO_2 NA and the excellent electron-transport characteristic of SnO_2 NS, by controlling the ratio of NA to NS. Consequently, the DSCs fabricated with TPS2, in which 50 wt% SnO_2 NSs was introduced in the SnO_2 hybrid film, achieved the highest PCE of 5.59%, a remarkable 54.8% improvement compared to that of the corresponding cell fabricated with bare SnO_2 NAs photoanode (sample TP). This work demonstrates that rationally designing a hybrid photoelectrode film could be a promising approach to enhance the efficiency of SnO_2-based DSCs.

Supplementary Materials: The following are available online at http://www.mdpi.com/1996-1944/11/9/1774/s1, Figure S1: SEM image of SnO_2 NAs.

Author Contributions: D.W. and S.L. designed the experiments; M.S., J.Z. and Y.G. carried out the experiments; Q.L. and X.Z. analyzed the data; D.W. wrote the paper; J.Z. and Y.F. review and edited the paper.

Funding: This work was supported by the Shandong Province Natural Science Foundation of China (ZR2018LB032), Liaocheng University Funds for Young Scientists (31805), and the National Natural Science Foundation of China (51473074, 31400044).

Conflicts of Interest: The authors declare no conflict of interest.

References

1. Song, D.D.; Cui, P.; Wang, T.Y.; Xie, B.X.; Jiang, Y.J.; Li, M.C.; Li, Y.Y.; Du, S.; He, Y.; Liu, Z.H.; et al. Bunchy TiO_2 Hierarchical Spheres with Fast Electron Transport and Large Specific Surface Area for Highly Efficient Dye-Sensitized Solar Cells. *Nano Energy* **2016**, *23*, 122–128. [CrossRef]
2. Balasingam, S.K.; Kang, M.G.; Jun, Y. Metal Substrate based Electrodes for Flexible Dye-sensitized Solar Cells: Fabrication Methods, Progress and Challenges. *Chem. Commun.* **2013**, *49*, 11457–11475. [CrossRef] [PubMed]
3. Balasingam, K.S.; Jun, Y. Recent Progress on Reduced Graphene Oxide-Based Counter Electrodes for Cost-Effective Dye-Sensitized Solar Cells. *Isr. J. Chem.* **2015**, *55*, 955–965. [CrossRef]

4. Ko, K.W.; Lee, M.; Sekhon, S.S.; Balasingam, S.K.; Han, C.-H.; Jun, Y. Efficiency Enhancement of Dye-Sensitized Solar Cells by the Addition of an Oxidizing Agent to the TiO_2 Paste. *ChemSusChem* **2013**, *6*, 2117–2123. [CrossRef] [PubMed]
5. Ahn, S.H.; Kim, D.J.; Chi, W.S.; Kim, J.H. Hierarchical Double-Shell Nanostructures of TiO_2 Nanosheets on SnO_2 Hollow Spheres for High-Efficiency, Solid-State, Dye-Sensitized Solar Cells. *Adv. Funct. Mater.* **2014**, *24*, 5037–5044. [CrossRef]
6. Rui, Y.C.; Xiong, H.; Su, B.; Wang, H.Z.; Zhang, Q.H.; Xu, J.L.; Buschbaum, P.M. Liquid-liquid interface assisted synthesis of SnO_2 nanorods with tunable length for enhanced performance in dye-sensitized solar cells. *Electrochim. Acta* **2017**, *227*, 49–60. [CrossRef]
7. Dadkhah, M.; Salavati, N.M. Controlled Synthesis of Tin Dioxide Nanostructures via Two Simple Methods and the Influence on Dye Sensitized Solar Cell. *Electrochim. Acta* **2014**, *129*, 62–68. [CrossRef]
8. Shalan, A.E.; Rasly, M.; Osama, I.; Rashad, M.M.; Ibrahim, I.A. Photocurrent Enhancement by Ni^{2+} and Zn^{2+} Ion Doped in SnO_2 Nanoparticles in Highly Porous Dye-Sensitized Solar Cells. *Ceram. Int.* **2014**, *40*, 11619–11626. [CrossRef]
9. Wijeratne, K.; Alilavasan, J.; Thelakkat, M.; Bandara, J. Enhancing the Solar Cell Efficiency through Pristine 1-Dimentional SnO_2 Nanostructures: Comparison of Charge Transport and Carrier Lifetime of SnO_2 Particles vs. Nanorods. *Electrochim. Acta* **2012**, *72*, 192–198. [CrossRef]
10. Xing, J.; Fang, W.Q.; Li, Z.; Yang, G.H. TiO_2-Coated Ultrathin SnO_2 Nanosheets Used as Photoanodes for Dye-Sensitized Solar Cells with High Efficiency. *Ind. Eng. Chem. Res.* **2012**, *51*, 4247–4253. [CrossRef]
11. Bai, Y.; Yu, H.; Li, Z.; Amal, R.; Lu, G.Q.; Wang, L.Z. In Situ Growth of a ZnO Nanowire Network within a TiO_2 Nanoparticle Film for Enhanced Dye-Sensitized Solar Cell Performance. *Adv. Mater.* **2012**, *24*, 5850–5856. [CrossRef] [PubMed]
12. Balasingam, S.K.; Lee, M.; Kang, M.G.; Jun, Y. Improvement of Dye-Sensitized Solar Cells toward the Broader Light Harvesting of the Solar Spectrum. *Chem. Commun.* **2013**, *49*, 1471–1487. [CrossRef] [PubMed]
13. Dong, Z.H.; Ren, H.; Hessel, C.M.; Wang, J.Y.; Yu, R.B.; Jin, Q.; Yang, M.; Hu, Z.D.; Chen, Y.F.; Tang, Z.Y.; et al. Quintuple-shelled SnO_2 Hollow Microspheres with Superior Light Scattering for High-Performance Dye-Sensitized Solar Cells. *Adv. Mater.* **2014**, *26*, 905–909. [CrossRef] [PubMed]
14. Dou, X.C.; Sabba, D.; Mathews, N.; Wong, L.H.; Lam, Y.M.; Mhaisalkar, S. Hydrothermal Synthesis of High Electron Mobility Zn-doped SnO_2 Nanoflowers as Photoanode Material for Efficient Dye-Sensitized Solar Cells. *Chem. Mater.* **2011**, *23*, 3938–3945. [CrossRef]
15. Cho, C.Y.; Baek, S.; Kim, K.; Moon, J.K. 3D bicontinuous SnO_2/TiO_2 Core/Shell Structures for Highly Efficient Organic Dye-Sensitized Solar Cell Electrodes. *RSC Adv.* **2016**, *6*, 74003–74008. [CrossRef]
16. Zheng, Y.Z.; Zhao, J.X.; Bi, S.Q.; Tao, X.; Huang, M.L.; Chen, J.F. Dual Interfacial Modifications of Hierarchically Structured Iodine-doped ZnO Photoanodes for High-Efficiency Dye-sensitized Solar Cells. *Electrochim. Acta* **2015**, *157*, 258–265. [CrossRef]
17. Wali, Q.; Fakharuddin, A.; Ahmed, I.; Rahim, M.H.A.; Ismail, J.; Jose, R. Multiporous nanofibers of SnO_2 by electrospinning for high efficiency dye-sensitized solar cells. *J. Mater. Chem. A* **2014**, *2*, 17427–17434. [CrossRef]
18. Bai, Y.; Xing, Z.; Yu, H.; Li, Z.; Amal, R.; Wang, L.Z. Porous titania nanosheet/nanoparticle hybrids as photoanodes for dye-sensitized solar cells. *ACS Appl. Mater. Interfaces* **2013**, *5*, 12058–12065. [CrossRef] [PubMed]
19. Cai, F.S.; Yuan, Z.H.; Duan, Y.Q.; Bie, L.J. TiO_2 coated SnO_2 Nanosheet Flms for Dye-Sensitized Solar Cells. *Thin Solid Films* **2011**, *519*, 5645–5648. [CrossRef]
20. Bhande, S.S.; Shinde, D.V.; Tehare, K.K.; Patil, S.A.; Mane, R.S.; Naushad, M.; Alothman, Z.; Hui, K.N.; Han, S.H. DSSCs Synergic Effect in Thin Metal Oxide Layer-Functionalized SnO_2 Photoanodes. *J. Photochem. Photobiol. A Chem.* **2014**, *295*, 64–69. [CrossRef]
21. Wang, Y.J.; Tian, J.J.; Fei, C.B.; Lv, L.L.; Liu, X.G.; Zhao, Z.X.; Cao, G.Z. Microwave-Assisted Synthesis of SnO_2 Nanosheets Photoanodes for Dye-Sensitized Solar Cells. *Phys. Chem. C* **2014**, *118*, 25931–25938. [CrossRef]
22. Yang, S.; Hou, Y.; Xing, J.; Zhang, B.; Tian, F.; Yang, X.H.; Yang, H.G. Ultrathin SnO_2 scaffolds for TiO_2-based Heterojunction Photoanodes in Dye-Sensitized Solar Cells: Oriented Charge Transport and Improved Light Scattering. *Chem. Eur. J.* **2013**, *19*, 9366–9370. [CrossRef] [PubMed]
23. Lu, X.H.; Zheng, Y.Z.; Bi, S.Q.; Wang, Y.; Tao, X.; Dai, L.M.; Chen, J.F. Multidimensional ZnO Architecture for Dye-Sensitized Solar Cells with High-Efficiency up to 7.35%. *Adv. Energy Mater.* **2014**, *4*, 1301802. [CrossRef]

24. Wang, Y.F.; Li, J.W.; Hou, Y.F.; Yu, X.Y.; Su, C.Y.; Kuang, D.B. Hierarchical Tin Oxide Octahedra for Highly Efficient Dye-Sensitized Solar Cells. *Chem. Eur. J.* **2010**, *16*, 8620–8625. [CrossRef] [PubMed]
25. Zhao, Q.R.; Xie, Y.; Dong, T.; Zhang, Z.G. Oxidation-Crystallization Process of Colloids: An Effective Approach for the Morphology Controllable Synthesis of SnO_2 Hollow Spheres and Rod Bundles. *J. Phys. Chem. C* **2007**, *111*, 11598–11603. [CrossRef]
26. Wang, D.T.; Liu, S.H.; Shao, M.F.; Li, Q.Y.; Gu, Y.K.; Zhao, J.H.; Zhang, X.X.; Zhao, J.S.; Fang, Y.Z. Aqueous Solution-Processed Multifunctional SnO_2 Aggregates for Highly Efficient Dye-Sensitized Solar Cells. *Ind. Eng. Chem. Res.* **2018**, *57*, 7136–7145. [CrossRef]
27. Roh, K.M.; Kim, S.K.; Choi, J.H. Synergetic Effect of Graphene Sheet and Three-Dimensional Crumpled Graphene on the Performance of Dye-Sensitized Solar Cells. *AIChE J.* **2016**, *62*, 574–579. [CrossRef]
28. Xu, X.Q.; Qiao, F.J.; Dang, L.Y.; Lu, Q.Y.; Gao, F. Porous Tin Oxide Nanosheets with Enhanced Conversion Efficiency as Dye-Sensitized Solar Cell Electrode. *J. Phys. Chem. C* **2014**, *118*, 16856–16862. [CrossRef]
29. Lu, Z.; Zeng, L.; Song, W.L.; Qin, Z.Y.; Zeng, D.W.; Xie, C.S. In situ synthesis of C-TiO_2/g-C_3N_4 heterojunction nanocomposite as highly visible light active photocatalyst originated from effective interfacial charge transfer. *Appl. Catal. B Environ.* **2017**, *202*, 489–499. [CrossRef]
30. Zhang, Y.; Zhao, Z.Y.; Chen, J.R.; Cheng, L.; Chang, J.; Sheng, W.C.; Hu, C.Y.; Cao, S.S. C-doped hollow TiO_2 spheres: In situ synthesis, controlled shell thickness, and superior visible-light photocatalytic activity. *Appl. Catal. B Environ.* **2015**, *165*, 715–722. [CrossRef]
31. Gubbala, S.; Russell, H.B.; Shah, H.; Deb, B.; Jasinski, J.; Rypkemac, H.; Sunkara, M.K. Surface Properties of SnO_2 Nanowires for Enhanced Performance with Dye-Sensitized Solar Cells. *Energy Environ. Sci.* **2009**, *2*, 1302–1309. [CrossRef]
32. Gubbala, S.; Chakrapani, V.; Kumar, V.; Sunkara, M.K. Band-Edge Engineered Hybrid Structures for Dye-Sensitized Solar Cells Based on SnO_2 Nanowires. *Adv. Funct. Mater.* **2008**, *18*, 2411–2418. [CrossRef]
33. Cahen, D.; Hodes, G.; Grätzel, M.; Guillemoles, J.F.; Riess, I. Nature of Photovoltaic Action in Dye-Sensitized Solar Cells. *J. Phys. Chem. B* **2000**, *104*, 2053–2059. [CrossRef]
34. Lee, M.; Balasingam, K.S.; Ko, Y.; Jeong, H.Y.; Min, B.K.; Yun, Y.J.; Jun, Y. Graphene Modified Vanadium pentoxide Nanobelts as an Efficient Counter Electrode for Dye-Sensitized Solar Cells. *Synth. Met.* **2016**, *215*, 110–115. [CrossRef]
35. Adachi, M.; Sakamoto, M.; Jiu, J.; Ogata, Y.; Isoda, S. Determination of Parameters of Electron Transport in Dye-Sensitized Solar Cells Using Electrochemical Impedance Spectroscopy. *J. Phys. Chem. B* **2006**, *110*, 13872–13880. [CrossRef] [PubMed]
36. Zheng, Y.Z.; Ding, H.Y.; Liu, Y.; Tao, X.; Cao, G.Z.; Chen, J.F. In situ Hydrothermal Growth of Hierarchical ZnO Nanourchin for High-Efficiency Dye-Sensitized Solar Cells. *J. Power Sources* **2014**, *254*, 153–160. [CrossRef]
37. Wang, D.T.; Wang, W.X.; Ma, X.Y.; Zhang, C.; Zhao, J.S.; Zhang, X.X. Comparative Study on the Influence of TiO_2 Precursors on ZnO-Based Dye-Sensitized Solar Cells. *Ind. Eng. Chem. Res.* **2015**, *54*, 12639–12645. [CrossRef]
38. Tian, J.J.; Zhang, Q.F.; Zhang, L.L.; Gao, R.; Shen, L.F.; Zhang, S.G.; Qu, X.H.; Cao, G.Z. ZnO/TiO_2 Nanocable Structured Photoelectrodes for CdS/CdSe Quantum Dot Co-Sensitized Solar Cells. *Nanoscale* **2013**, *5*, 4362–4369. [CrossRef] [PubMed]
39. Zhang, Q.F.; Chou, T.P.; Russo, B.; Jenekhe, S.A.; Cao, G.Z. Aggregation of ZnO Nanocrystallites for High Conversion Efficiency in Dye-Sensitized Solar Cells. *Angew. Chem.* **2008**, *120*, 2436–2440. [CrossRef]
40. Zhang, X.L.; Huang, W.C.; Gu, A.N.; Xiang, W.C.; Huang, F.Z.; Guo, Z.X.; Cheng, Y.B.; Spiccia, L. High Efficiency Solid-State Dye-Sensitized Solar Cells Using a Cobalt(II/III) Redox Mediator. *J. Mater. Chem. C* **2017**, *5*, 4875–4883. [CrossRef]
41. Zhu, P.N.; Reddy, M.V.; Wu, Y.Z.; Peng, S.J.; Yang, S.Y.; Nair, A.S.; Lohd, K.P.; Chowdari, B.V.R.; Ramakrishna, S. Mesoporous SnO_2 Agglomerates with Hierarchical Structures as An Efficient Dual- Functional Material for Dye-Sensitized Solar Cells. *Chem. Commun.* **2012**, *48*, 10865–10867. [CrossRef] [PubMed]